Applied Energy 291 (2021) 116473

Contents lists available at ScienceDirect

Applied Energy

journal homepage: www.elsevier.com/locate/apenergy

Experimental analysis and analytical modeling of Enhanced-Ragone plot

Edoardo Catenaro [a], Denise M. Rizzo [b], Simona Onori [a,*]

[a] Department of Energy Resource Engineering, Stanford University, 367 Panama St, Stanford, CA 94305, United States
[b] U.S. Army CCDC Ground Vehicle Systems Center, 6501 E. 11 Mile Road, Warren, MI 48397, United States

HIGHLIGHTS

- Lithium-ion batteries (NCA, NMC and LFP) galvanostatic discharge experiments.
- Battery characterization C-rate: C/20 - 15C and Temperature: 5–45 °C.
- Testing over multiple samples for statistical significance analysis.
- Enhanced-Ragone plot design and experimentally derived spider plot.
- Modeling and experimental validation for specific energy vs specific power relation.

ARTICLE INFO

Keywords:
Lithium-ion battery
Enhanced-Ragone plot
Analytical power-energy relationship
Battery galvanostatic tests
Statistical characterization of battery data

ABSTRACT

In this study, we propose an experimentally validated Enhanced-Ragone plot (ERp) that displays key characteristics of lithium-ion batteries (LIBs) in terms of their cathode composition and operating conditions, and can be employed as a design tool to guide energy storage system (ESS) selection for applications ranging from electrified vehicles to stationary grid storage. We build the ERp using experiments - under different C-rate and operating temperature - from cylindrical graphite anode LIBs of the type 1865 nickel-cobalt-aluminum-oxide, 2170 nickel-manganese-cobalt-oxide and 2665 iron-phosphate. Moreover, for each LIB tested, six cell samples are used to assess the statistical significance and repeatability of the data collected. A zero-th order equivalent circuit-based modeling approach is then proposed and experimentally validated to predict the specific energy and specific power on the ERp. Finally, the proposed ERp framework is showed on a case study of battery sizing in electric vehicle applications.

1. Introduction

Due to their higher specific energy and energy density and continuously reducing cost, lithium-ion batteries (LIBs) have shown to be a key technology to transitioning away from fossil fuel, by enabling high market penetration of hybrid-electric vehicles (HEVs) and electric vehicles (EVs) [1]. Over the last decade, LIB have reduced their cost from $1160/kWh in 2010 to $176 kWh in 2018 [2] while enhancing their performance [3] resulting in a continuously appealing technology for a wide range of applications, from road-transport to stationary grid-storage.

However, one of the main drawbacks of this technology is that they suffer from aging, both calendar and cycle, which hinders long term operation and performance [4].

On the other hand, supercapacitors (SCs) are energy storage systems (ESSs) that can provide up to millions of cycles to the targeted application without losing performance along the way. This, combined with high specific power and low internal resistance, makes them an appealing storage device for transport electrification and stationary grid storage application, such as frequency regulation service. Nonetheless, the low volumetric energy and the high cost of raw materials [5] still make SCs a not-market-ready solution at large.

The road-transport sector has exploited the potential of SCs for high-specific power vehicle maneuvers (such as start-stop, strong accelerations, kinetic energy recovery, among others). Literature works have proposed hybrid ESS (HESS) architectures in which the battery pack is connected in parallel with SCs thus lowering the peak power absorption and dissipation from the battery, hence mitigating battery degradation and improving the overall powertrain efficiency [6]. In [7], an integrated design and control optimization framework is applied to a series

* Corresponding author.
E-mail addresses: cedoardo@stanford.edu (E. Catenaro), sonori@stanford.edu (D.M. Rizzo), denise.m.rizzo2.civ@mail.mil (S. Onori).

https://doi.org/10.1016/j.apenergy.2021.116473
Received 16 April 2020; Received in revised form 30 December 2020; Accepted 10 January 2021
Available online 21 March 2021

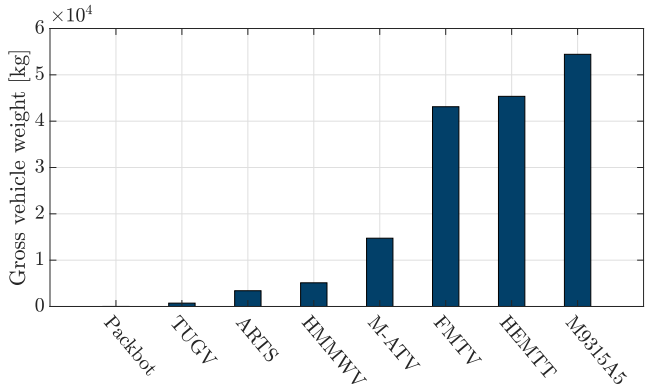

Fig. 1. Military vehicles by gross weight. From the left (lighter) to the right (heavier): packbot small-class robotics [10], tactical unmanned ground vehicle (TUGV) [11], all-purpose remote transport system (ARTS) [12], high mobility multipurpose wheeled vehicle (HMMWV) [13], mine-resistant ambush protected all-terrain vehicle (M-ATV) [14], family medium tactical vehicle (FMTV) [15], heavy expanded mobility tactical truck (HEMTT) [16] and line haul tractor M9315A5 [17].

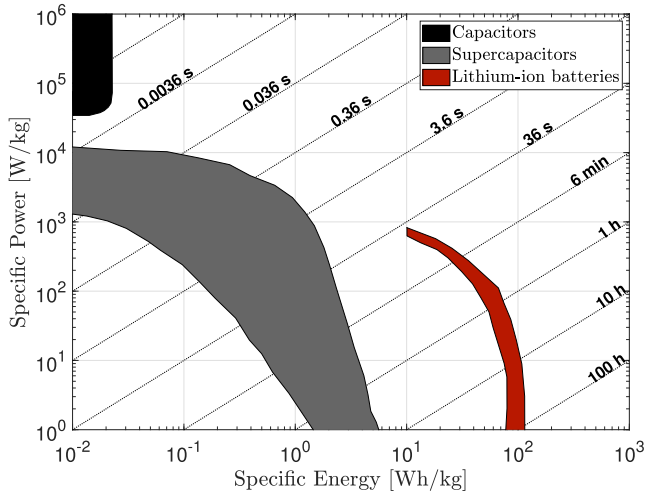

Fig. 2. Ragone plot displaying capacitors, SCs and LIBs. Diagonal lines correspond to the time required to extract/store energy from/to the device. Data are from [19].

hybrid electric military truck with an internal combustion engine (ICE) and HESS.

Automakers rely on a "one-solution-fits-all" approach for the selection of ESS, which is typically a LIB with graphite anode and lithium-nickel-manganese-cobalt-oxide (NMC) cathode for electric vehicles. Given the restricted variation in load requirements and operating conditions of the vehicle fleet, this results in the most suitable approach from an engineering and economic standpoint. On the contrary, if the application at hand is characterized by a vast range of targeted performances, then the selection of the most appropriate ESS is to be addressed case-by-case.

A typical example of such a case is the electrification of military vehicles (MVs). Unlike passenger vehicles, the variation in load requirements, mission objectives and operating conditions experienced by MVs makes the energy storage selection task particularly challenging [8]. US Army vehicles span from 11.2 kg packbot to $50{\cdot}10^3$ kg tactical trucks. Fig. 1 shows the ground military fleet by gross weight. While a fuel cell/battery system might be chosen to power packbots, for large tanks instead a powertrain containing an ICE and a HESS (LIB plus SC) could be more suitable. Moreover, load requirements as well as

Table 1
Comparison of typical LIBs and SCs performance [5] at ambient operating temperature. The cycle life evaluation for a device considers one charge per day.

	LIBs	SCs
Specific energy [Wh/kg]	100–265	4–10
Volumetric energy [Wh/L]	220–400	4–14
Specific power [kW/kg]	4	3–40
Cycle life [years]	5–10	10–15
Efficiency [%]	75–90	98
Self-discharge [%/month]	2	40–50
Cost [$/kWh]	200–1000	10000

operating conditions (e.g., ground unevenness, working temperature) are mission-dependent. This in turn determines the stress, in terms of C-rate of operation and increase of temperature during operation, experienced by the ESS. For instance, a tactical truck used for cargo or moving heavy equipment will experience a largely different load than a tactical truck used for silent watch mission.

Energy storage systems used for grid-storage applications also experience a quite diverse range of usage, in terms of charge-discharge characteristics, temperature and power vs energy requirements [9].

The ability to match targeted load requirements and vehicle characteristics with the most appropriate ESS candidate calls for a tool where ESS performance can be exhibited and compared according to some relevant characteristics. Such a tool is presented in this paper.

The Ragone plot (Rp), named after David V. Ragone [18], has been the most convenient way to capture and compare energy storage technologies in terms of their specific power [W/kg] and specific energy [Wh/kg], as shown in Fig. 2 where logarithmic scales are used to comprise a large range of ESS categories. The specific energy and specific power extracted by a given ESS are obtained by fully discharging the device from a fully charged condition.[1] The extracted energy and power depend on many factors, such as chemical composition, ambient temperature, discharge rate, aging, etc. It is common practice to identify on the Rp families of ESSs, as shown by the colored area in Fig. 2, the boundaries of which are determined by physical constraints of the storage device.

The time taken by the device to discharge, or *characteristic time*, is proportional to the energy-to-power ratio of the ESS (in the log-log plane the time corresponds to straight diagonal lines). High power can only be delivered for short amount of time, whereas high energy is obtained by devices that are characterized by a large energy-to-power ratio. Batteries are typically useful for medium/long time applications (order of hours), whereas SCs are more suitable for short time applications (order of seconds/minutes).

Unlike common capacitors, SCs (also referred to as electrochemical capacitors or ultracapacitors), do not use solid dielectric to separate the electrical conductors, but rather, they adopt electrostatic double-layer capacitance and electrochemical pseudocapacitance to store electric energy [20]. With that, higher specific energy (up to roughly 10 Wh/kg) is attained still maintaining high-power performance (40 kW/kg, under nominal conditions). SCs provide complementary characteristics to LIBs as they can satisfy higher peaks of power demand and guarantee a longer cycle life (typically in the order of millions of cycles [21]) and high efficiency (around 98%). Moreover, SCs are less susceptible to degradation at low and high temperatures [22]. On the downside, they have lower specific and volumetric energy (below 10 Wh/kg and 14 Wh/L, respectively), suffer of rapid self-discharge (up to 50 %/month) and their cost per kWh is around ten times the ones of LIBs [5]. The complementary performance of LIBs and SCs, summarized in Table 1, can provide an opportunity to design hybrid energy storage solutions to

[1] The Rp can also be populated with specific energy and specific power evaluated when the considered ESS is charged from fully discharged to fully charged condition.

combine the pros of both devices while mitigating the cons of each of them taken singularly.

In [23], the variation of electrochemical characteristics of a $LiCoO_2$ battery,[2] with respect to cell shape design, cylindrical or prismatic, were experimentally inspected and represented on the Rp. In [24], $LiNiCoAlO_2$/graphite and $LiNiMnCoO_2$ (one sample each) were tested at three different discharge rates ($1C, 3C$ and $5C$) and at various reference temperatures ($-20\,^{\circ}C, 0\,^{\circ}C, -25\,^{\circ}C$ and $55\,^{\circ}C$) and results mapped on Rp. In [25] a larger range of discharge rates ($C/5, C/2, 1C, 2C, 5C$ and $10C$) and reference temperatures ($-20\,^{\circ}C, 0\,^{\circ}C, -25\,^{\circ}C$ and $55\,^{\circ}C$) were tested on one sample of $LiCoO_2$battery. In [26], the following discharge experiments (i) $C/10, 1C, 3C$ and $4.6C$ at $25\,^{\circ}C$ and $-10\,^{\circ}C$; (ii) moderate discharge rate of $1C$ at different reference temperatures ($-20\,^{\circ}C, -10\,^{\circ}C, 0\,^{\circ}C, 25\,^{\circ}C$ and $45\,^{\circ}C$) were performed over a single NMC cell sample.

Rp has been employed as a selection tool to determine suitable ESSs for a given application. In [27], an optimization algorithm is outlined to determine whether a nickel-metal-hybrid battery or a SC or their combination are most suitable for a HEV. In [28], a similar methodology is used to choose between lead-acid battery and SC and find a suitable size of the two devices from the Rp. Rp has also been used to select ESSs in a wind power farm [29]. In all these works, though, the Rp does not carry information about the ESSs performance under different C-rate, temperature and across different LIBs.

In this paper, three LIBs are investigated: lithium-nickel-cobalt-aluminum-oxide (NCA), NMC and lithium-iron-phosphate (LFP). For each LIB, six samples were tested starting from 100% state-of-charge (SOC) and under controlled temperatures ($5\,^{\circ}C, 25\,^{\circ}C$ and $35\,^{\circ}C$), and galvanostatic discharge rates of:

- $C/20, 1C, 2C, 3C, 5C$ for NCA and NMC batteries,
- $C/20, 1C, 2C, 3C, 5C, 10C, 15C, 20C$ for LFP battery.

Along with specific power and energy calculations, battery cell capacity, surface temperature, discharge efficiency and the relative discharge time are also calculated to thoroughly characterize the three LIBs. For the three LIBs tested, the goal is to systematically define specific energy and specific power in terms of temperature and C-rate of operation and across multiple samples.

We experimentally build the *Enhanced-Ragone plot* (ERp) with the purpose of using it as a tool to select ESSs to match the requirements of a targeted application by looking beyond just the specific energy and specific power content of the storage device.

Moreover, we propose a model capable to replicate the power-energy relationship found experimentally on the ERp.

Few literature works have addressed this topic. In [30], the proposed power-energy relationship emphasized the ESSs losses: 1) ohmic polarization losses and 2) kinetic polarization (Tafel) losses. Simulation results showed the impact of the losses parameters variation on the energy/power performance (represented on the Rp). Similarly, in [31], authors attempted to define a quantitative method to model a large set of ESSs (battery, capacitors, flywheel, etc.). For instance, batteries were modeled as an electric circuit involving a capacitor, an internal series resistance and a leakage resistance. Based on such a model the power-energy relationship is analytically computed allowing a sensitivity study on the Rp. In [32], authors proposed a battery model composed of an open-circuit potential (analytically expressed as a function of the battery SOC) and an internal resistance. The capacity is expressed as function of the discharge current through the Peukert's law. The whole set of model parameters are taken from manufacturer data. In particular, potential and capacity related parameters are inferred from the voltage versus time discharge behavior of the battery. As also stated by the authors, the determination of this process might be subjective and inexact. In [33], a first order dynamical model was proposed to capture the specific energy versus specific power of Hitachi LIB used for HEV applications, where the open-circuit voltage was taken as a constant value representing the average value of the whole curve.

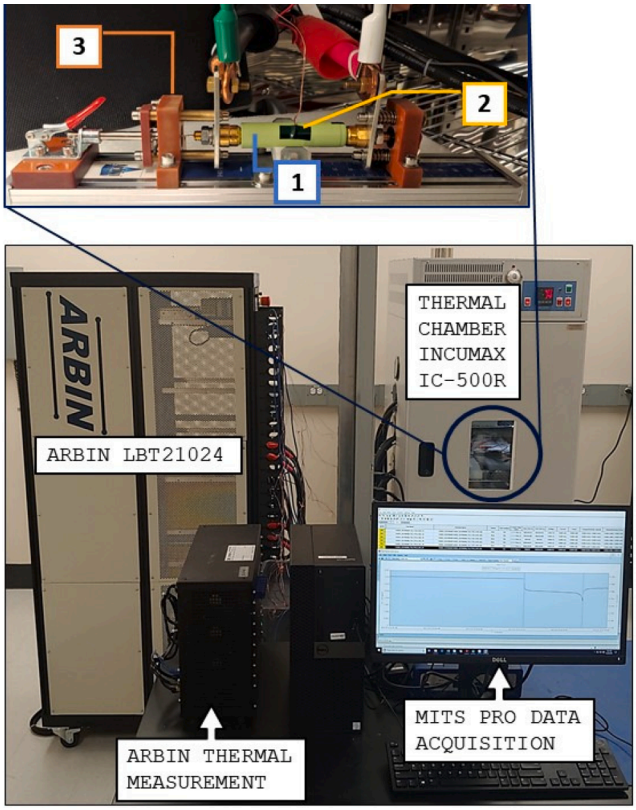

Fig. 3. Experimental test setup at the Stanford Energy Control Laboratory. The top figure shows a battery fixture (3) holding an NCA cell (1) with a T-type thermocouple sensor positioned on it (2) positioned in the thermal chamber and connected to the Arbin cycler.

The aforementioned works lacks experimental validation. In this paper, the analytical power-to-energy relationship based on an equivalent circuit model of the battery, is experimentally validated on the ERp. The applicability of the proposed ERp modeling approach is verified in a case study dealing with the sizing of battery pack in an EV.

The main contributions of this paper are summarized as follows:

- Comprehensive characterization of three LIBs. Battery cell capacity, surface temperature, discharge efficiency and discharge time are analyzed according to different discharge rates and operating temperatures for multiple battery samples. Energy and power performance are mapped on the ERp.
- Experimentally derived spider plot showing the comparison of the three LIBs tested in this work based on the five performance metrics.
- Analytical model and its experimental validation of a LIB power-energy relationship based on zero-th order equivalent circuit model and a single experiment for parameter identification. The modeling approach is tested on a real case study aiming at the battery selection and sizing in EV application.

The paper is organized as follows. Section 2 describes the design of experiments and the experimental testing campaign. In Section 3, the experimental data is processed and quantities of interest, such as specific power and specific energy, are used to build the ERp. In Section 4 the analytical power-to-energy relationship is derived and experimentally validated on the ERp, and used in a real world application. Finally,

[2] We refer to LIB by only specifying their cathode chemical composition, with the underlying assumption that graphite is used at the anode.

Table 2
Technical specifications of the Arbin battery test system, thermal chamber and Arbin thermal measurement system.

Laboratory equipment	Manufacturer technical specifications	
Arbin battery test system	Manufacturer	Arbin Instruments
	Model	LBT21024
	Number of channels	6
	Voltage range [V]	0–5
	Current ranges [A]	±0.5, ±5, ±50 and ± 250
	Maximum continuous output power [W]	1250
	Measurement resolution	24-bit
	Simulation control	Current/Power simulation
	Auxiliaries	Temperature measurement
	AC Power input	{3-Phase 50/60 Hz 208 VAC
		Input power: 17400 VA
Thermal chamber	Manufacturer	Amerex Instrument
	Model	IncuMax IC-500R
	Interior volume [m^3]	0.5
	Temperature range [°C]	−5 to 55
	Temperature accuracy [°C]	±0.1
	Temperature uniformity [°C]	±1 at 37
	Power input	1-Phase 50/60 Hz 120 VAC
Arbin thermal measurement system	Manufacturer	Amerex Instrument
	Model	LBT21024
	Voltage [V]	90 −264
	Maximum current	220 V, 1.6 A/ 110 V, 3.2 A
	Maximum power [VA]	350
	Phase	1

Section 5 gathers the conclusions of this study.

2. Experimental setup

Experiments were carried out at the Stanford Energy Control Laboratory, Energy Resources Engineering Department, Stanford University. The experimental setup, showed in Fig. 3, is composed of the Arbin LBT21024 with a programmable power supply, the IncuMax IC-500R thermal chamber for temperature controlled experiments, T_{amb}, the Arbin thermal measurement system used to measure cell surface temperature data from thermocouples placed on the cell; a MITS Pro and Data Watcher software to program test profiles and monitor real-time

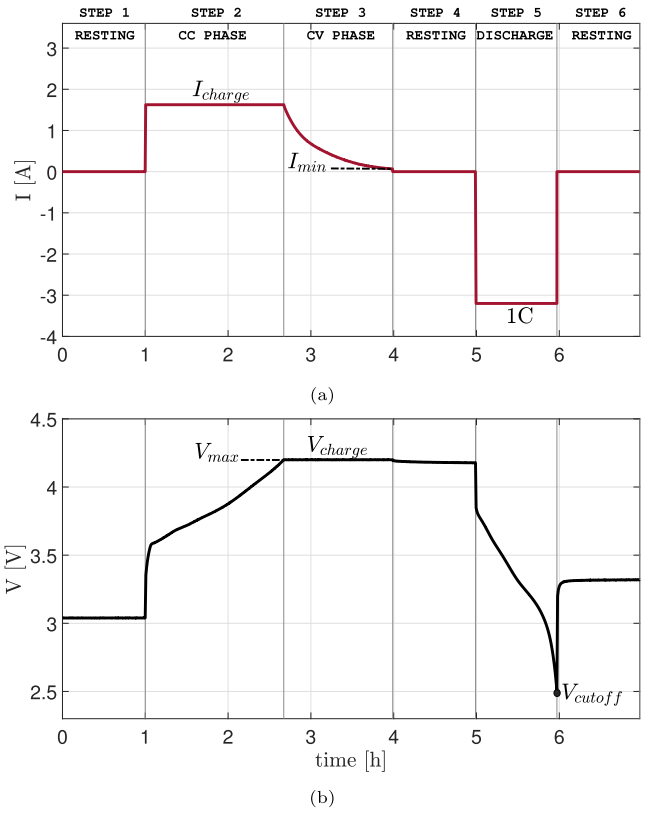

Fig. 4. (a) Current and (b) voltage profiles during the galvanostatic discharge test for NCA battery cell tested at 1*C* and 25 °C. Each step of the test protocol is highlighted and separated by a gray vertical line.

Table 3
Manufacturer specifications for the NCA [34], NMC [35] and LFP [36] cylindrical battery cells used in this work.

	NCA	NMC	LFP
Cathode chemistry composition	$LiNiCoAlO_2$	$LiNiMnCoO_2$	$LiFePO_4$
Anode chemistry composition	graphite	graphite	graphite
Manufacturer	Panasonic	LG Chem	A123 Systems
Manufacturer model	NCR-18650B	INR21700-M50	ANR26650m1-B
Size (diameter x length) [mm x mm]	18.5 x 65.3	21.1 x 70.15	26 x 65
Weight $M_{nom,cell}$ [g]	47.5	68	76
Nominal voltage V_{nom} [V]	3.6	3.63	3.3
Nominal capacity Q_{nom} [Ah]	3.35	4.85	2.5
Charging voltage V_{charge} [V]	4.2	4.2	3.6
Charging current I_{charge} [A]	1.625	1.455	2.5
Cut-off voltage V_{cutoff} [V]	2.5	2.5	2
Charging cut-off voltage V_{max} [V]	4.2	4.2	3.6
Max. constant discharge current $I_{dis,max}$ [A]	6.7 (2C)	7.275 (1.5C)	50 (20C)

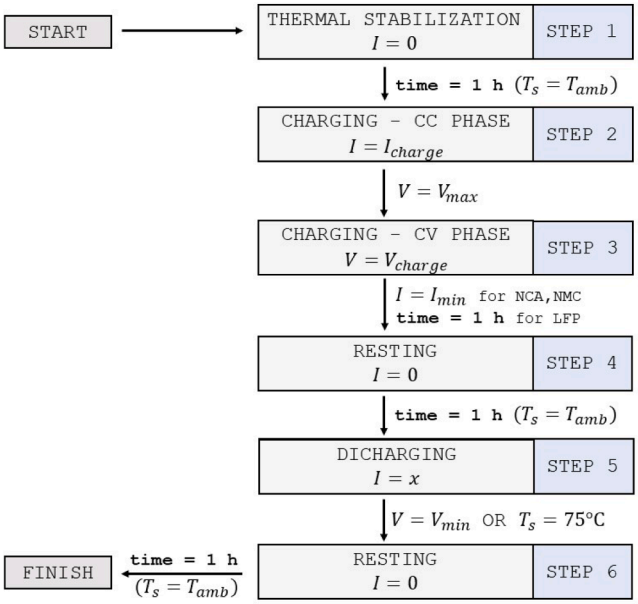

Fig. 5. Discharge procedure flowchart. For every step - represented as a rectangular gray box - the controlled variable is indicated along with its assigned value. The transition from one step to the next takes place when the condition on one of the three measured signal is satisfied. x indicates the value of the applied C-rate, which varies with the experiment.

data. Technical specifications of the Arbin LBT21024, the IncuMax IC-500R and the Arbin thermal measurement system are reported in Table 2. The following signals are measured: cell current, I, cell voltage, V, and cell surface temperature, T_s. The latter is measured with a type-T thermocouple sensor, manufactured by Omega, and transmitted through the Arbin auxiliary channel to the thermal measurement system.

In this work, we investigate three different LIBs whose manufacturer specifications are listed in Table 3. Moreover, for each LIB, six samples are available for testing. In what follows, we refer to the specific LIB by the variable $b, b = \{\text{NCA, NMC, LFP}\}$, and the given sample by the index $k, k = \{1, \ldots, 6\}$.

For the purpose of building the ERp, constant discharge experiments are conducted. Fig. 4 shows a typical current and voltage profile from the current discharge test preceded by the constant current - constant voltage (CC-CV) phase implemented to bring the battery at 100% SOC while the temperature was being kept at $T_{amb} = 25$ °C.

The experimental testing procedure is described in the flowchart of Fig. 5. In Step 1, one hour rest time period ($I = 0$) is enforced to bring the cell at the desired temperature[3] $T_s = T_{amb}$. In Step 2 and 3, the standard charging protocol CC-CV is applied. During the CC phase the cell is subjected to the constant current I_{charge}, specified by the manufacturer, until the voltage reaches the charging cut-off value V_{max} (as listed in Table 3). In the CV phase the cell is kept at constant voltage V_{charge}.[4] One hour rest time is enforced in Step 4 at the end of which the cell is fully charged and thermally stable. In Step 5, a given discharge current value, specified in terms of C-rate, x, is commanded until the voltage reaches the discharge cut-off value V_{cutoff} (reported in Table 3). In case the cell surface temperature hits the thermal limit of 75 °C the discharge phase is immediately ended. The set of C-rates used is LIB-dependent (summarized in Table 4). For each LIB the following temperatures are tested, namely 5 °C, 25 °C and 35 °C at the various C-rate. Finally, one hour resting time is allowed in Step 6 to thermally stabilize the cell after the discharge phase. Step 1 to 6 are repeated for each experiment.

[3] The time to synchronize the tested battery cell temperature with the target temperature results to be always less than one hour, however the one hour rest time guarantees experimental reliability.

[4] For NCA and NMC batteries, the CV phase ends as soon as the current becomes lower than a fixed current cut-off value I_{min} of 65 mA and 50 mA, respectively. LFP technical specifications recommend to end the CV phase after 60 min.

Table 4
Values of applied C-rates, x, for each LIB chemistry.

Variable	Description	Battery	Values
x	C-rate	NCA	$C/20, 1C, 2C, 3C, 5C$
		NMC	$C/20, 1C, 2C, 3C, 5C$
		LFP	$C/20, 1C, 2C, 3C, 5C, 10C, 15C, 20C$

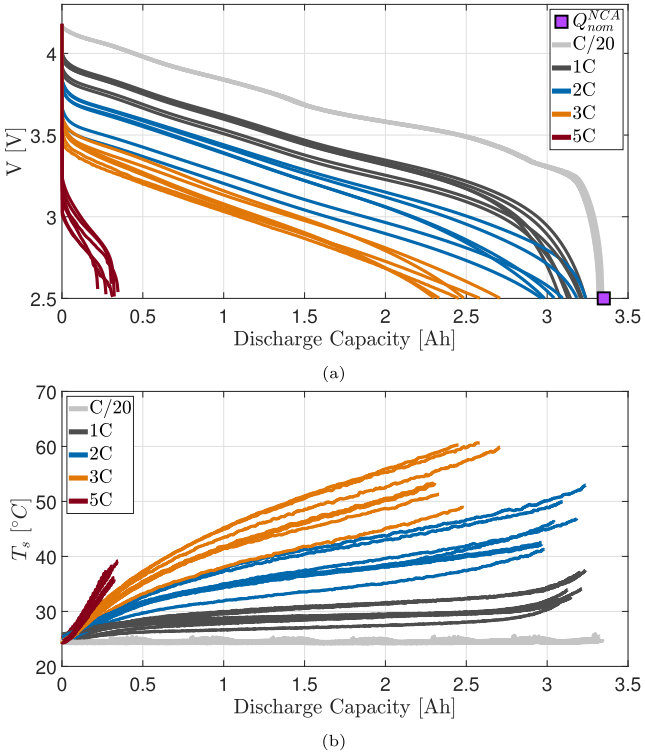

Fig. 6. Voltage to discharge capacity behavior for six NCA cell samples at ambient temperature $T_{amb} = 25$ °C and for different discharge rates: $C/20, 1C$, $2C, 3C$ and $5C$. The value of Q_{nom}^{NCA} corresponds to the manufacturer nominal capacity of NCA battery which is obtained under C/20 discharge at 25 °C.

Fig. 6 shows the voltage (a) and surface temperature (b) to discharge capacity for the six NCA cells tested at a controlled temperature $T_{amb} = 25$ °C. NMC and LFP batteries exhibit similar behaviors. The discharge capacity of a given battery b and cell sample $k, Q^{b,k}$, is obtained by time integration of the measured cell current, $I^{b,k}$,

$$Q^{b,k} = \int_0^{t_f^{b,k}} I^{b,k} dt, \tag{1}$$

where $t_f^{b,k}$ is the final discharge time of battery b and cell sample k. The mean capacity value, μ, from the cell samples, Q^b, is given by:

$$Q^b = \frac{\sum_{k=1}^{6} Q^{b,k}}{6} = \mu\left[Q^{b,k}\right]. \tag{2}$$

Fig. 7a shows the mean capacity for the three chemistry under study as a function of C-rate for different testing temperatures. Also, on the same plot the nominal capacity value (as provided by the manufacturer, see Table 3) is reported.

As one can see, the mean capacity value obtained at $C/20$ and $T_{amb} =$

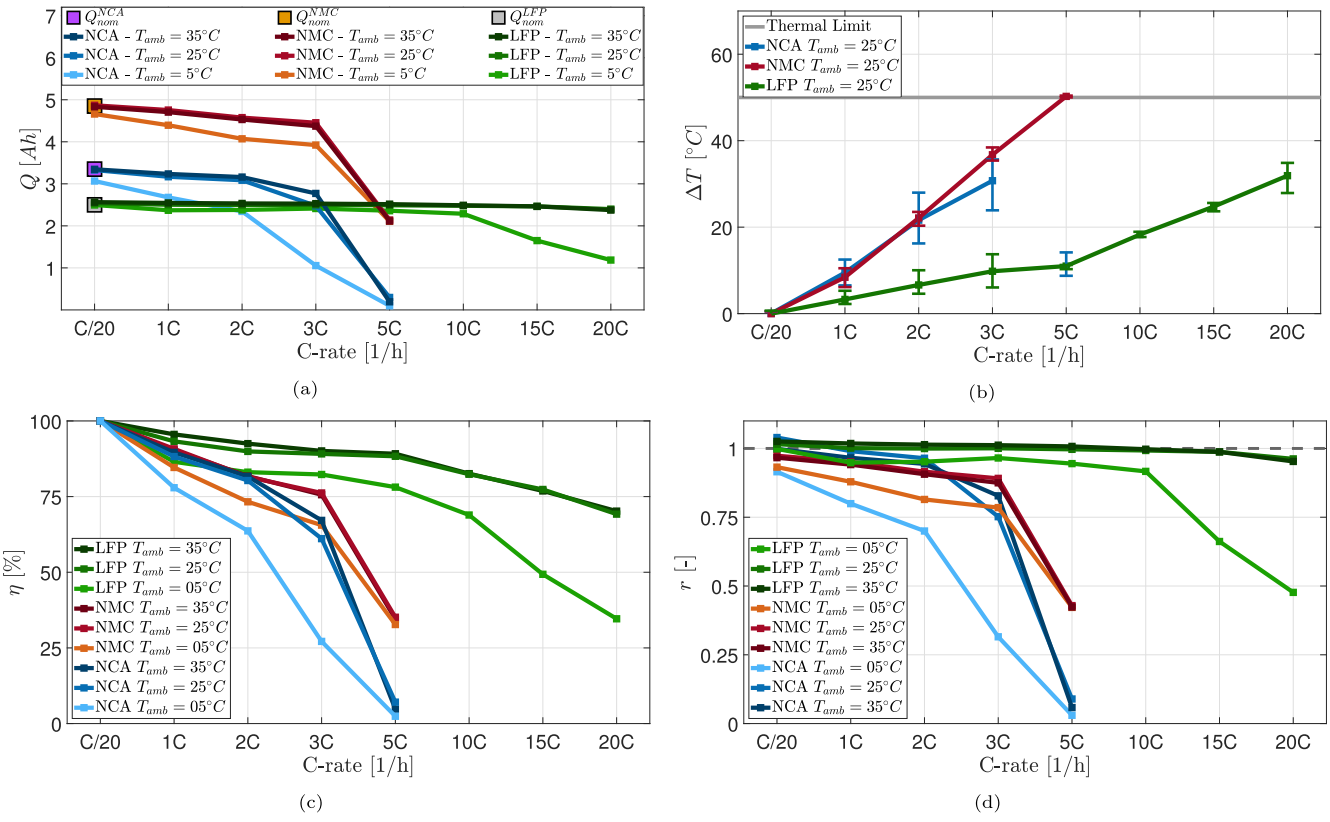

Fig. 7. (a) Capacity Q, computed from Eq. 2, (b maximum cell surface temperature increment ΔT, from Eq. 4, (c discharge efficiency η_{pk}, from Eq. 5, and (d) relative discharge time r, from Eq. 9, for NMC, NCA and LFP batteries, as a function of C-rate and ambient temperature. Figure (b) shows data only for 25 °C. In the figure, each ΔT point is associated to a vertical bar whose upper and lower limits are the minimum and maximum cell surface temperature increment across the six cell samples.

Table 5
Maximum cell surface temperature increment [°C], computed with Eq. 4. Red values are related to conditions where the thermal limit of 75 °C was reached.

Cell surface temperature increment	Reference temperature	Discharge rates C/20	1C	2C	3C	5C	10C	15C	20C
ΔT^{NCA} [°C]	$T_{amb} = 5°C$	0.84	13.80	29.12	22.79	5.19			
	$T_{amb} = 25°C$	0.03	9.49	21.61	30.73	12.01			
	$T_{amb} = 35°C$	0	8.21	20.41	27.86	5.43			
ΔT^{NMC} [°C]	$T_{amb} = 5°C$	1.72	17.30	22.27	31.51	35.07			
	$T_{amb} = 25°C$	0.10	8.40	22.13	36.73	50.25			
	$T_{amb} = 35°C$	0.01	9.74	16.95	29.51	39.97			
ΔT^{LFP} [°C]	$T_{amb} = 5°C$	2.40	6.72	12.17	16.98	15.97	22.06	19.61	18.44
	$T_{amb} = 25°C$	0	3.27	6.62	9.80	11	18.29	24.75	31.91
	$T_{amb} = 35°C$	0	2.10	5.04	7.74	7.56	14.77	20.94	26.20

25 °C is consistent with the manufacturer nominal capacity.[5]

The constant discharge current applied to the cell makes their surface cell temperature increase throughout the duration of the experiment. We define cell surface temperature increment, $\Delta T^{b,k}$, as the maximum value of the difference between the cell surface temperature, $T_s^{b,k}(t)$ (for battery b and cell sample k), and the ambient temperature, T_{amb}, across the overall galvanostatic discharge window. Since the surface temperature increases monotonically, then the maximum value of such an increment is obtained at $t = t_f$, hence

$$\Delta T^{b,k} = T_s^{b,k}(t_f) - T_{amb}. \tag{3}$$

For each battery chemistry, the average value of the cell surface temperature increment is given by:

$$\Delta T^{b} = \mu\left[\Delta T^{b,k}\right]. \tag{4}$$

As the discharge rate increases the cell generates more heat. Power losses caused by Joule heating are given by I^2R, where R corresponds to the cell internal resistance [24]. In this paper, we define *thermal*

[5] The considered operating conditions - $C/20$ discharge rate and $T_{amb} = 25$ °C - satisfy manufacturer nominal conditions for NCA and NMC chemistry. On the other hand, LFP nominal working conditions, given by manufacturer, correspond to a C-rate of $C/2$ and $T_{amb} = 25$ °C. Nevertheless, under these nominal conditions the LFP measured capacity is consistent with the nominal capacity provided by the manufacturer.

robustness the ability of the battery to limit its internal heat generation.

Fig. 7b depicts the cell surface temperature increment, ΔT^b, experienced by the three chemistry under different C-rates and controlled operating temperature of 25 °C (other temperatures exhibit similar behaviors which are summarized in Table 5). Each point in the figure is plotted together with its upper and lower temperature values experienced across the six cell sample. One can notice how, in some cases, the temperature spread across the same batch can result in a quite significant temperature difference. It is worth remarking that as the cells are connected in series and/or parallel in a battery module or pack, such a spread can be a source of a significant temperature gradient within the pack, leading to heterogeneous pack aging [37].

LFP cells have higher thermal robustness across all C-rates, as opposed to NCA and NMC, which on the other hand are subject to increase internal heat loss linearly with C-rate. This is due to a greater internal resistance owned by NCA and NMC batteries. In facts, parameter identification conducted in Section 4 shows a value of the LFP internal resistance around three times smaller than NMC and five times smaller than NCA battery, respectively. NCA cells show an unusual temperature behavior when tested at 5*C* discharge rate.[6] In fact, when tested at such high C-rate the time of discharge, experimentally observed, is shorter than the theoretically calculated discharge time. Such an inconsistency takes place when the discharge rate reaches or exceeds the manufacturer recommendations,[7] like in this case.

The discharge efficiency of battery b, undergoing to a discharge rate x, controlled at temperature T_{amb}, is computed as follows

$$\eta^b_{pk}\left(x, T_{amb}\right) = \frac{W^b\left(x, T_{amb}\right)}{W^b\left(C/20, T_{amb}\right)}, \tag{5}$$

where the normalization term, $W^b(C/20, T_{amb})$ is the energy released by the battery b, at ambient temperature T_{amb}, discharged at $C/20$ (corresponding to the baseline released energy value), whereas W^b is the mean of the released energy computed across the k samples, $W^{b,k}$, given as

$$W^b = \mu\left[W^{b,k}\right], \tag{6}$$

where $W_{b,k}$ is calculated as follows

$$W^{b,k} = \int_0^{t_f^{b,k}} V^{b,k} I^{b,k} dt. \tag{7}$$

The discharge efficiency defined in this paper is related to the Peukert-like effect [38] where the discharge energy at a given C-rate is measured against the discharge energy at $C/20$. As the rate of discharge increases, the battery's available energy decreases, according to the Peukert's effect.

The results obtained for the discharge efficiency are plotted in Fig. 7c. Moreover, LFP cells show higher efficiency than NMC and NCA for the same C-rate and across all the C-rate tested. This is due to the their higher thermal robustness. Lastly, the lower the operating temperatures, the more is the reduction of the discharge efficiency.

Next, we analyze the *relative discharge time*, which reveals an interesting correlation with the thermal properties of each battery. The time of discharge associated with the applied C-rate (e.g., 1 h for 1*C*, 30 min for 2*C* and so forth) is a theoretical assumption.

The actual discharge time of the cell is found to be dependent on the cell sample, the electrode chemical composition, and ambient temperature.

A relation between the theoretical and the actual time of discharge is proposed. The theoretical discharge time, referred to as t^b_x, only depends on the applied C-rate, which, in turn, depends on the nominal capacity of a given battery b. The actual discharge time for the battery b is taken as the average across the six samples

$$t^b\left(x, T_{amb}\right) = \mu\left[t^{b,k}\left(x, T_{amb}\right)\right], \tag{8}$$

where $t^{b,k}$ corresponds to the actual discharge time of battery b and cell sample k. The relative discharge time, r, is defined as the ratio between t^b and t^b_x

$$r^b\left(x, T_{amb}\right) = \frac{t^b\left(x, T_{amb}\right)}{t^b_x}. \tag{9}$$

Fig. 7d shows the ratio r as a function of the applied discharge rate and temperature, for each chemistry. It is shown that r takes up a value close to 1 only at $C/20$, irrespective to the cell chemistry and temperature. Higher discharging rates emphasize the dependence of r on the C-rate and temperature of operation. The reduction in discharge time of NCA and NMC is due to the low thermal robustness of these two electrode chemistry as compared to LFP. For instance, at 5*C* discharge rate (corresponding to a theoretical discharge time of 12 min) at 25 °C, the NCA and NMC are discharged in 1 min, 3.6 seconds, and 9 min, 22.2 seconds, respectively.[8] On the other hand, LFP cells are able to maintain, for every applied C-rate and ambient temperatures greater than 25 °C, an actual discharge time comparable to the theoretical one. Lower temperatures contribute to further reduce the value of r across all C-rates.

3. Enhanced-Ragone plot

In this section, the experimental design of the ERp is discussed. The specific energy for the battery type b and cell sample k, undergoing to a discharge rate x at a controlled at temperature T_{amb}, is computed as follows

$$w^{b,k}\left(x, T_{amb}\right) = \frac{W^{b,k}\left(x, T_{amb}\right)}{M^b_{nom,cell}}, \tag{10}$$

where $W^{b,k}$, is the released energy computed from Eq. 7 and $M^b_{nom,cell}$ is the cell nominal mass of battery b (noted in Table 3). Hence the specific energy for each battery b is taken by averaging the specific energy values over the six samples as

$$w^b\left(x, T_{amb}\right) = \mu\left[w^{b,k}\left(x, T_{amb}\right)\right]. \tag{11}$$

The specific power of battery b and cell sample k is computed as follows

$$p^{b,k}\left(x, T_{amb}\right) = \frac{w^{b,k}\left(x, T_{amb}\right)}{t^{b,k}_f}, \tag{12}$$

where $w^{b,k}$ is obtained from Eq. 10. The denominator of Eq. 12 corresponds to the overall time of discharge. Finally, the specific power of battery type b is

$$p^b\left(x, T_{amb}\right) = \mu\left[p^{b,k}\left(x, T_{amb}\right)\right]. \tag{13}$$

The obtained average values of specific energy w^b and specific power p^b are a function of the applied discharge rate, x, and operating ambient temperature, T_{amb}.

[6] Differently from NCA cells, the cell surface temperature increment of NMC cells maintains its trend hitting the thermal limit of 75 °C (triggering the stop of the experiment).

[7] The maximum constant discharge current is given by manufacturer specifications and corresponds to 1.45*C* for NCA, 1.5*C* for NMC and 20*C* for LFP. The proposed experimental tests exceed these limits to provide a more exhaustive description of the cell dynamic behavior.

[8] Under 5*C* discharge rate, the corresponding r value for NCA and NMC, respectively, is similar across all tested temperatures. This is due to a remarkably short discharge time measured for NCA cells, whereas NMC cells ends their discharge approximately at the same time.

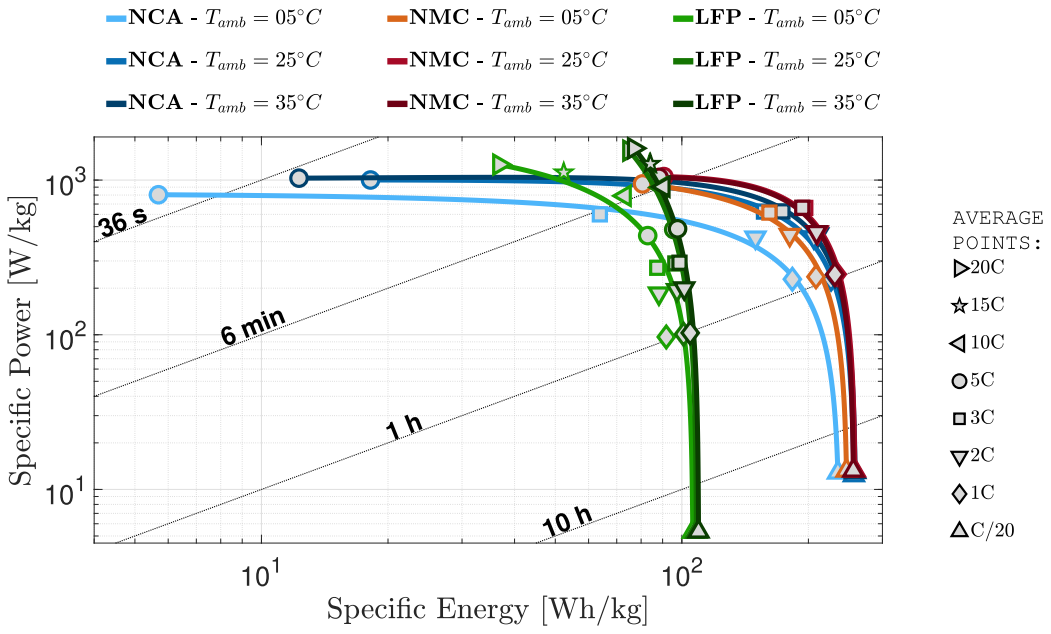

Fig. 8. ERp displaying the specific power versus specific energy performance of NCA, NMC and LFP cells at different ambient temperatures and discharge rates (listed in Table 4).

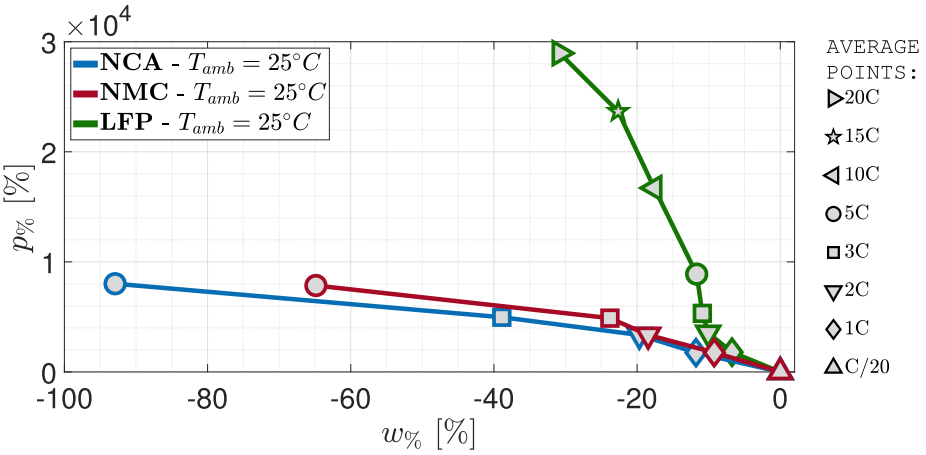

Fig. 9. Relative increment of specific power, $p_{\%}$, versus the relative decrement of specific energy, $w_{\%}$, under different discharge rate and at given temperature of 25 °C.

From the galvanostatic discharge experiments discussed in the previous section, w^b and p^b are being calculated in a logarithmic scale and plotted in the ERp of Fig. 8.

The LIBs performance in the ERp shows the typical hooked-shape behavior where the increase of the delivered power is possible at the cost of a reduction in the retained energy. The specific energy stored in NCA and NMC cells is approximately as twice as much the one in the LFP (for discharge rates below 2C). However, LFP can retain higher specific power across much larger C-rate range of operation. In fact, LFP cells can support high C-rate (up to 20C) without disrupt the cell regular behavior. Differently, NCA and NMC can only operate over a limited C-rate range to prevent high Joule losses and rapid drop in voltage response, resulting in reduced specific power capability.

The three electrochemical cells under study show a similar trend to the variation of ambient temperature. Both achievable specific power and specific energy are reduced at low temperature conditions (especially for higher C-rates).

From the ERp, one can also calculate the relative increment/decrement of specific energy and specific power upon an increase of C-rate. For a given C-rate, x, temperature, T_{amb}, and according to the battery type b, we define the relative percent variation of specific energy, $w^b_{\%}$, and specific power, $p^b_{\%}$, with respect to the baseline case (corresponding to $C/20$) as

$$w^b_{\%}\left(x, T_{amb}\right) = \left[\frac{w^b(x, T_{amb}) - w^b(C/20, T_{amb})}{w^b(x, T_{amb})}\right] \cdot 100, \tag{14}$$

$$p^b_{\%}\left(x, T_{amb}\right) = \left[\frac{p^b(x, T_{amb}) - p^b(C/20, T_{amb})}{p^b(x, T_{amb})}\right] \cdot 100. \tag{15}$$

As the operating C-rate increases from the baseline of $C/20$, thre three electrochemical cells show an increment of specific power and decrement of specific energy. Yet, such variations are strongly dependent on the electrode chemical composition and skewed towards a more pronounced decreased in energy than increase of power. For example, for a discharge rate of 5C, the increment in specific power is around $+8{\cdot}10^3$% for the three cells, whereas the decrement of specific energy is more pronounced for NCA, -93%, and NMC, -65%, and quite limited for LFP, -12%. (Fig. 9)

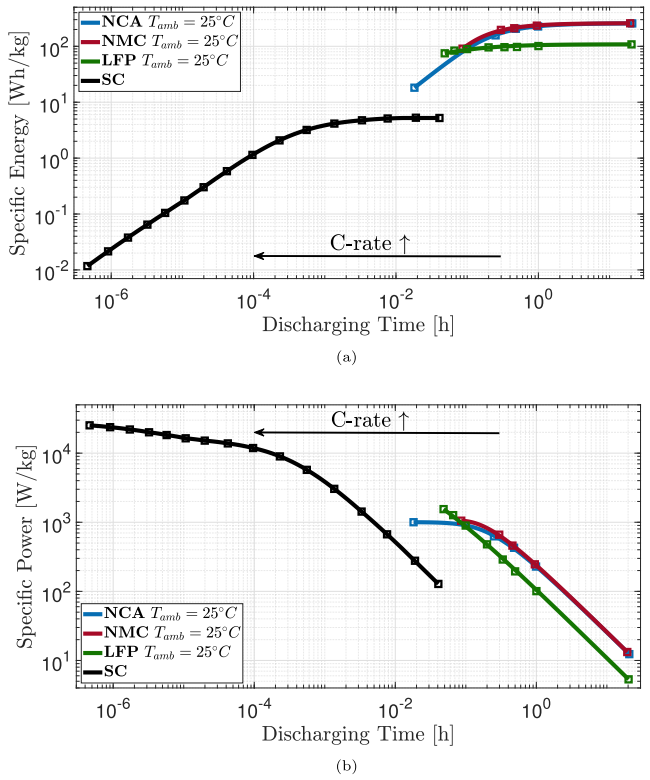

Fig. 10. Representation of the specific energy (a) and specific power (b) with respect to the theoretical discharge time on log-log planes for LIBs and SC BCAP0350.

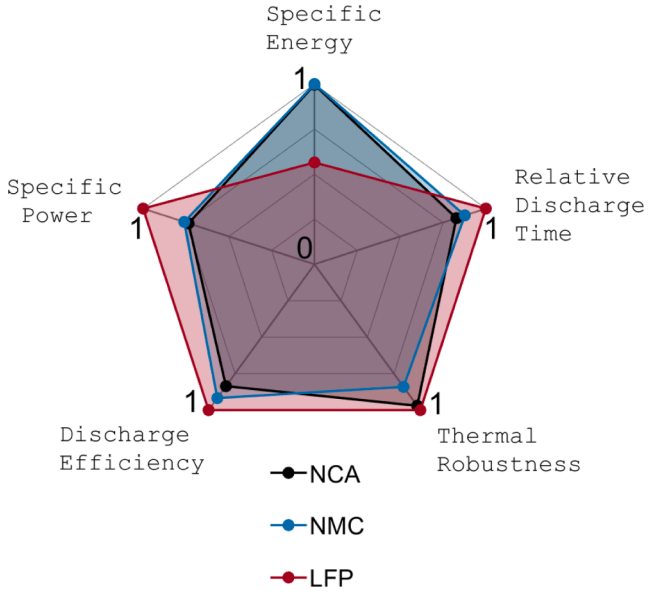

Fig. 11. Spider plot showing the normalized performance of NCA, NMC and LFP in terms of specific energy, specific power, discharge efficiency, thermal robustness and relative discharge time.

Along with LIBs, performance of SCs are also addressed. In particular, in this study, the BCAP0350 SC [39] is analyzed and compared against LIBs using the SC manufacturer data. SCs are known for their specific power superiority compared to LIBs. Inversely, batteries are able to store a greater amount of energy per unit mass, that can be delivered over a longer time interval. This difference is highlighted in Fig. 10 where the two classes of devices show complimentary characteristics. If

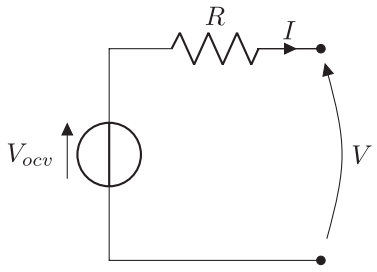

Fig. 12. Zero-th electric circuit model.

a fast power release capability is requested along with high specific energy, then the integration of these two technologies in the form of HESS architecture could provide a valuable solution. An example of such an application is discussed in [40], where the SCs are employed for the start-up maneuver of the vehicle while the battery guarantees a satisfying energy tank.

Finally, to summarize the LIB features analyzed thus far, the spider plot shown in Fig. 11 is proposed where specific energy, specific power, discharge efficiency, relative discharge time and thermal robustness[9] are shown. The specific energy and specific power are taken from their respective maximum values across the tested C-rates, while the discharge efficiency, thermal robustness and relative discharge time are evaluated based on the average across the tested C-rates. Each metric is normalized with respect to its corresponding "best case" and scaled from 0 to 1 (where 1 corresponds to the "best case"). Fig. 11 shows that NCA and NMC have similar performance (only thermal robustness is slightly different), whereas LFP cells do better than NMC and NCA on all metrics except specific energy.

4. ERp modeling

In this section, we propose a modeling approach to replicate the battery performance on the ERp. To this aim, we define the battery power-to-energy relationship employing the zero-th electric circuit model showed in Fig. 12. The circuit includes a voltage source V_{ocv}, that is the open-circuit voltage of the cell, and a series resistor R, representing the cell internal losses. The variables V and I are the cell voltage and current, where positive current indicates discharge and negative current charge.

The objective is to express the power delivered by the battery cell as a function of the stored energy. This task is split in a three-steps procedure described below.

Step 1: Energy-current relationship

The energy stored in the cell, W, is expressed as follows

$$W = Q \cdot V = Q \cdot (V_{ocv} - IR), \tag{16}$$

where Q is the cell nominal capacity. Parameters Q, R and V_{ocv} are assumed to be constant values, not depending on time and the applied discharge current I is constant. Based on these assumptions, Eq. 16 expresses a static relationship between the amount of stored energy in the battery and the discharge current.

Eq. 16 can be rewritten as

$$I = \frac{-1}{R} \cdot \left(\frac{W}{Q} - V_{ocv} \right). \tag{17}$$

Step 2: Energy-power relationship

The power delivered to the load, P, is expressed as follows

[9] This metric provides an evaluation of the battery thermal robustness based on experimental data from cell surface temperature measurements. Good thermal robustness corresponds to lower values of cell surface temperature increment (Eq. 4).

Table 6
Model parameters and corresponding tests to be performed to identify the power-to-energy analytical relationship defined in Eq. 22.

Parameter	Assignment criteria
R	Current train-pulse discharge test
V_{ocv}	Current train-pulse discharge test
Q	Nominal capacity (manufacturer specifications)
M_{cell}	Nominal cell mass (manufacturer specifications)

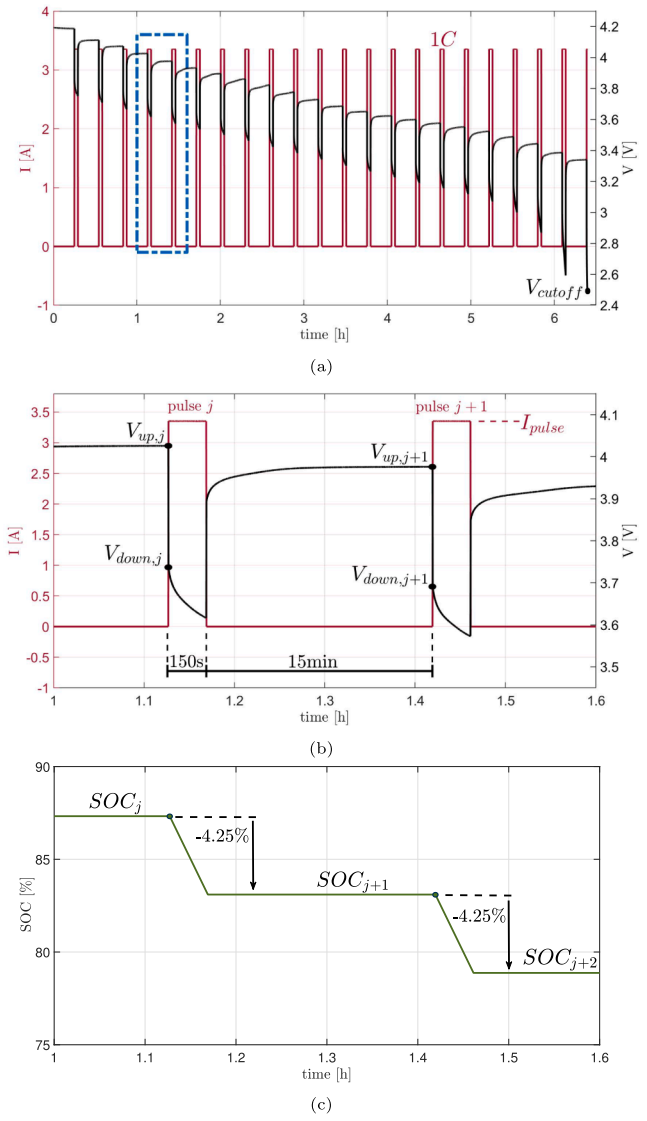

Fig. 13. Current pulse-train discharge profile and corresponding voltage response (a) of NCA cell at an ambient temperature of 25 °C. The profiles framed by the dashed-blue rectangle are zoomed in (b), where two consecutive current pulses and their voltage response are shown, and the corresponding *SOC* behavior is depicted (c).

$$P = I{\cdot}V = I{\cdot}(V_{ocv} - IR) = IV_{ocv} - I^2R. \tag{18}$$

The term IV_{ocv} is the electrochemical power of the cell, and I^2R the internal power losses. Substituting Eq. 17 into 18, we obtain the power-energy relationship

$$P = \frac{V_{ocv}}{RQ}{\cdot}W - \frac{1}{RQ^2}{\cdot}W^2. \tag{19}$$

The derivation of Eq. 19 is in Appendix A.

Step 3: Specific energy-specific power relationship

For the power-energy relationship of Eq. 19 to be plotted in the ERp all variables must be expressed per unit mass. The specific energy, w, and the specific power, p, of the battery cell are defined as

$$W = w{\cdot}M_{cell}, \tag{20}$$

$$P = p{\cdot}M_{cell}. \tag{21}$$

Substituting Eq. 20 and 21 into 19 leads to

$$p = \frac{V_{ocv}}{RQ}{\cdot}w - \frac{M_{cell}}{RQ^2}{\cdot}w^2. \tag{22}$$

Eq. 22 describes the static power-energy relationship of a generic LIB battery undergoing a constant current discharge behavior. The specific power depends on the specific energy through a quadratic expression. The parameters involved are R, V_{ocv}, Q and M_{cell} which are being identified from experiments reported in Table 6.

4.1. Electric circuit parameters estimation

For a given battery, the parameters R and V_{ocv} to be used in Eq. 22 are estimated by means of a current pulse-train discharge test from a fully charged condition where the discharge pulses are at 1C and triggered every 15 min. Each pulse has a duration of 150 s. As soon as the cell voltage goes below the cut-off voltage V_{cutoff} (value reported in Table 3) the pulse discharge cycle is stopped.

Fig. 13a shows the current pulse-train profile and voltage response for NCA battery at 25 °C. A zoom of the profile during the fourth and fifth pulse is shown in Fig. 13b, and the corresponding *SOC* behavior is reported in Fig. 13c. The *SOC* of each battery type b and cell sample k is computed as follows

$$SOC^{b,k} = \frac{Q^b_{nom} - \int_0^{t_f^{b,k}} I^{b,k}dt}{Q^b_{nom}}. \tag{23}$$

The SOC reduction after each pulse is 4.25%.

The internal resistance R is calculated over the instantaneous voltage drop occurring in correspondence of every current pulse. It is calculated by taking the ratio between the voltage and the current difference across the pulse front. The value of R is a function of the cell *SOC*. With reference to Fig. 13c the value of internal resistance R computed for the j-th current pulse is as follows

$$R\left(SOC_j\right) = \frac{V_{up,j} - V_{down,j}}{I_{pulse}} \qquad j = \left\{1, \ldots, N\right\}, \tag{24}$$

where $V_{up,j}$ and $V_{down,j}$ are the measured voltage before and after the voltage drop at the current pulse j; I_{pulse} is the current pulse amplitude and SOC_j is the computed *SOC* value before the j-th pulse has occurred (this means that $SOC_{j=1} = 100\%$, battery fully charged before the first pulse) and N is the total number of current pulses.

After each discharge current pulse the cell voltage relaxes and reaches a lower steady-state value. The open-circuit voltage is estimated as the voltage measured after the relaxation dynamics caused by the current pulse j, which corresponds to $V_{up,j+1}$,

$$V_{ocv}\left(SOC_j\right) = V_{up,j+1}. \tag{25}$$

For battery chemistry b and cell sample k, the estimated parameters are noted as $R^{k,b}$ and $V^{k,b}_{ocv}$. The mean values of the estimated $R^{k,b}$ and $V^{k,b}_{ocv}$ with respect to the *SOC* variation are used in Eq. 22,

$$\overline{R^{k,b}} = \mu\left[R^{k,b}\left(SOC^{k,b}\right)\right], \tag{26}$$

$$\overline{V^{k,b}_{ocv}} = \mu\left[V^{k,b}_{ocv}\left(SOC^{k,b}\right)\right]. \tag{27}$$

The current pulse discharge experiment is performed for every

Table 7
Identified values of model parameters used in the analytical power-energy relationship (Eq. 22) for the three LIBs.

Model	Variable	NCA	NMC	LFP
parameters				
R [Ω]	$\overline{R^b}$	0.099	0.059	0.021
V_{ocv} [V]	$\overline{V^b_{ocv}}$	3.742	3.746	3.277
Q [Ah]	Q^b_{nom}	3.35	4.85	2.5
M_{cell} [g]	$M^b_{cell,nom}$	47.5	68	76

$$e^b_w\left(x\right) = \frac{\left|w^b(x) - \widehat{w}^b(x)\right|}{w^b(x)} \cdot 100, \tag{30}$$

$$e^b_p\left(x\right) = \frac{\left|p^b(x) - \widehat{p}^b(x)\right|}{p^b(x)} \cdot 100. \tag{31}$$

The bar plots in Fig. 15 gathers the specific energy and power RPE values, for each chemistry across all the tested C-rate. When considering the average from the RPE values taken across all the C-rate of operation, we obtain an average RPE of 4.88% for specific energy and 1.85% for the specific power for NCA, 2.93% and 1.44% for NMC, and 4.46% and 0.08% for LFP.

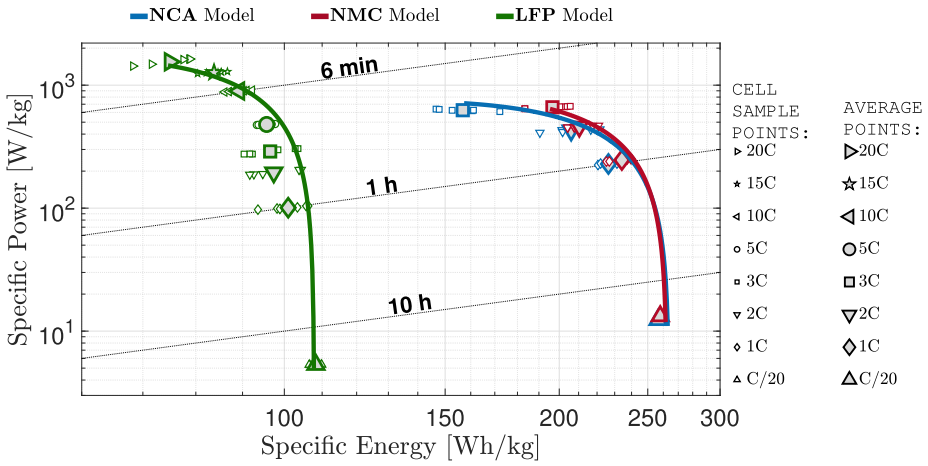

Fig. 14. Validation on the ERp plane of the analytical power-energy relationship for NCA, NMC and LFP batteries at different discharge rates and at 25 °C. Experimental data points of each cell sample as well as their average for each C-rate are also shown.

sample and the resulting estimated parameters are computed as the mean value from the batch of six cell samples in order to reduce the intrinsic variability associated to cell manufacturing process

$$\overline{R^b} = \mu\left[\overline{R^{k,b}}\right], \tag{28}$$

$$\overline{V^b_{ocv}} = \mu\left[\overline{V^{k,b}_{ocv}}\right]. \tag{29}$$

The set of parameters involved in the analytical power-energy relationship (Eq. 22) are listed in Table 7 for the three LIB tested.

The validation is conducted over data collected at 25 °C. The ERp plane in Fig. 14 is populated with: 1) the set of experimental data points obtained from each cell sample of the three LIBs tested under all discharge rates (listed in Table 4) at an ambient temperature of 25 °C ; 2) the average points from the six cell samples across the tested discharge rate at 25 °C; 3) the analytical power-energy relationship (Eq. 22) for each LIB (solid lines).

The validation results are assessed through the relative percent error (RPE) given as the difference between the experimental point and the corresponding model predicted point (under the same conditions), on the log-log specific energy specific power plane. For a given LIB, the experimental data point on the ERp - calculated by taking the average across the six cell samples[10] - is referred to as $w^b(x, T_{amb})$and $p^b(x, T_{amb})$ (Eqs. 11 and 13, respectively), and the corresponding point from the analytical power-energy relationship is defined by $\widehat{w}^b(x)$ and $\widehat{p}^b(x)$, respectively. Hence, for the battery type b, the specific energy and power RPE are

4.2. Case study

In this section, the proposed ERp power-energy relationship is applied to a use case related to battery pack sizing in an electric vehicle. The objective is to size the battery pack of a given vehicle based on performance requirements (e.g., range, driving cycle). We consider the Tesla model S (TMS) vehicle undergoing the urban dynamometer driving schedule (UDDS) [41] cycle repeated to travel a distance of 320 km. The objective is to 1) select the most adequate ESS to meet the vehicle requirements and 2) size the battery pack.

The selection of the most suitable battery chemistry involves the analysis of vehicle power requirement first and after the selection of the ESS on the ERp to match such requirements. A backward simulator of the TMS is employed [45] to compute the demanded power at the wheel, P_W, and, by time integration, the respective energy, E_W, as follows

$$P_W = \dot{x}\left(M_{veh}\ddot{x} + M_{veh}gsin\left(\delta\right) + \frac{1}{2}\rho_{air}A_f C_d \dot{x}^2\right), \tag{32}$$

$$E_W = \int_0^{t_f} P_W\, dt, \tag{33}$$

where $\dot{x}$ and $\ddot{x}$ are the vehicle velocity and acceleration, respectively, M_{veh} is the vehicle curb weight,[11] g is the gravitational time constant (9.81 m/s^2), f_r is the rolling friction coefficient (assumed to be constant), ρ_{air} is the air density (equal to 1 kg/m^3), A_f is the vehicle frontal area, C_d

[10] Statistical analysis of the voltage, capacity and internal resistance for the three LIBs from the pool of six samples is shown in Appendix B.

[11] Whole vehicle weight excluding passengers.

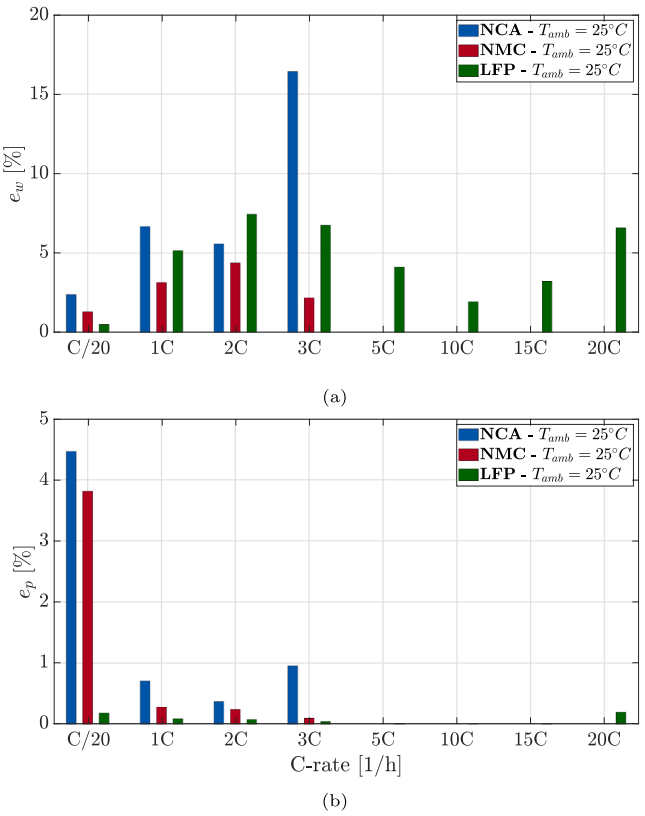

Fig. 15. RPE values in terms of (a) the specific energy, e_w^b, and (b) specific power, e_p^b, for different discharge rates at ambient temperature of 25 °C. The RPE values of NCA and NMC batteries are evaluated for $C/20, 1C, 2C$ and $3C$. The RPE values of LFP are calculated for up to $20C$.

Table 8
Vehicle parameter values for Tesla model S. Parameters M_{veh}, A_f, C_d are taken from [42], f_r from [43] and η from [44].

Vehicle	M_{veh} [kg]	A_f [m^2]	C_d [–]	f_r [–]	η [–]
Tesla model S	2087	2.34	0.24	0.012	0.8

is the drag coefficient and t_f is the time duration of the driving cycle.[12] From the power profile at the wheel, we move backward through the powertrain to characterize the power and energy required at the actuator. The battery-to-wheel powertrain efficiency, η, is approximately 80% [44]. TMS parameter values are summarized in Table 8. The power to the battery, P_B, and, by time integration, the respective energy during discharge, E_B, are computed as follows

$$P_B = \frac{1}{\eta} P_W, \tag{34}$$

$$E_B = \int_0^{t_f} P_B \, dt \qquad if \;\; P_B \geqslant 0. \tag{35}$$

With the purpose of translating vehicle requirements in terms of C-rate of operation, the (P/E) ratio during discharge associated to the battery is given as

$$\left(P \Big/ E\right) = \frac{P_B^*}{E_B}, \tag{36}$$

[12] The initial time is always assumed equal to 0.

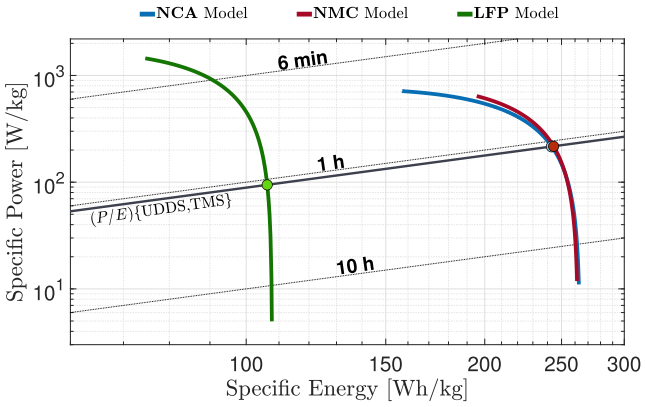

Fig. 16. ERp diagram populated with the analytical power-energy relationship of the LIBs - NCA, NMC and LFP - and the (P/E) ratio computed for the considered scenario (TMS over UDDS cycle for 320 km). Circle markers represent the intersection between the (P/E) ratio diagonal line and the LIB curves.

Table 9
Estimated battery pack weight (when no wiring, sensors and external case are included) and energy for NCA, NMC and LFP batteries for TMS application undergoing UDDS cycle for 320 km.

	NCA	NMC	LFP
$M_{pack,B}$ [kg]	278.5	277.4	638
$E_{pack,B}$ [Wh]	70.6	70.5	69.3

where P_B^* is the maximum battery discharge power.

The (P/E) ratio, computed with Eq. 36, has the unit of 1/h and can be represented with a diagonal line in the ERp log-log plane through the introduction of specific energy and power quantities. For the considered vehicle and driving cycle, the calculated (P/E) ratio is 0.88 1/h. Fig. 16 shows the ERp diagram with: 1) the analytical power-energy relationship (Eq. 22) and 2) the (P/E) ratio computed for the case study under study.

As showed in Fig. 16, the discharge rate corresponding to the computed (P/E) ratio can be handled by the three chemistry. The matching operation returns the intersection points over the LIB characteristic curves, namely $\overline{e}_B$ and $\overline{p}_B$. The coordinates of the selected ESS candidate are used to calculate the required mass of the device[13] as follows

$$M_{pack,B} = \max\left\{\frac{P_B^*}{\overline{p}_B}; \frac{E_B}{\overline{e}_B}\right\}. \tag{37}$$

From the required mass of the battery and given the cell nominal specific energy from manufacturer specification,[14] refer to as $e_{cell,B}$, the overall energy of the battery pack, $E_{pack,B}$, is computed as

$$E_{pack,B} = M_{pack,B}\, e_{cell,B}. \tag{38}$$

Results in terms of battery pack weight and energy - for each LIB - are summarized in Table 9. Based on each LIB cell nominal specific energy, the energy of the pack is computed accordingly.

[13] The computed ESS mass only considers the weight of the storage devices. Additional weight is needed to account for the metallic case and other components of the pack.

[14] When the cell nominal specific energy is not explicitly given in the datasheet, as for the NMC and LFP chemistry, we can compute it as the product between the cell nominal voltage and the cell nominal capacity, divided by the nominal cell mass.

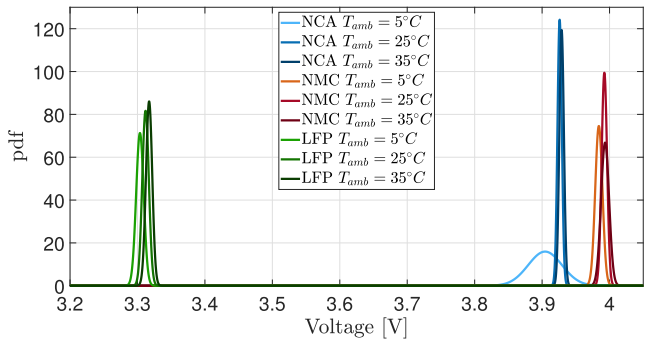

Fig. 17. Nominal voltage distributions calculated from the six cell samples for each LIB.

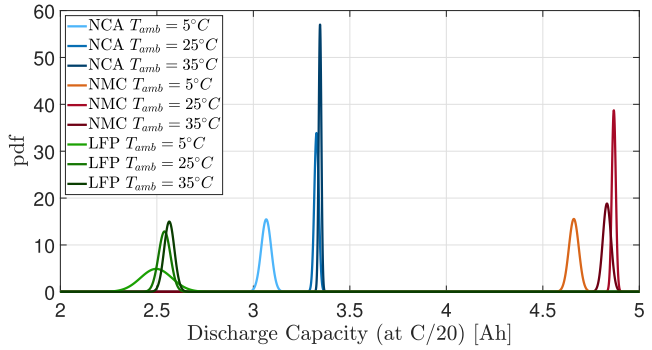

Fig. 18. Discharge capacity (at $C/20$) statistical distributions calculated from the six cell samples for each LIB.

5. Conclusions

This article investigated the experimental characterization of NCA, NMC and LFP cells in terms of their specific energy, specific power, thermal robustness, discharge efficiency and relative discharge time. Six fresh cell samples for each LIB were subjected to galvanostatic discharge at multiple C-rates and different temperatures. Analysis of experimental data shows that the NCA and NMC lose performance when tested at higher C-rates. Their poor thermal robustness results in an abrupt drop in measured capacity (up to −94% and −56%, respectively, when compared to their nominal value) and discharge efficiency (up to −95% and −65%, respectively, with respect to the $C/20$ baseline case). The measured cell surface temperature increment across the C-rates tested follows a similar trend for the NCA and NMC. Faster discharging rates do not disrupt the performance of LFP cells. The measured capacity remains close to the nominal value (the error never exceeds 5%), discharging efficiency is always greater than 70%, relative discharge time r is close to 1 (ideal case) and good thermal properties are showed (both in terms of thermal robustness and limited variation in temperature across different cell samples). Experimental data are used to construct the ERp. Despite the fact that previous works had proposed the construction of the ERp, with three LIBs used in this work along with multiple cell samples tested for each LIB and experiments covering a quite wide range of values of discharge rates, this work adds to the existing in our opinion.

Along with LIBs, SCs were also considered and compared against the LIBs on the ERp to highlight their complementary characteristics.

Next, we proposed a modeling approach intended to emulate the LIB behavior on the ERp. To this purpose, an analytical power-energy relationship and its experimental validation were proposed based on an equivalent electric circuit model whose parameters are estimated by means of a current pulse-train discharge experiment. Considering the discharging rates within manufacturer limit, NCA cells showed an RPE value of 4.88% for the specific energy and 1.85% for the specific power (for NMC, 2.93% and 1.44%; for LFP, 4.46% and 0.08%). Finally, the proposed ERp modeling procedure was applied to the problem of LIB selection and sizing for an EV application.

Declaration of Competing Interest

The authors declare that they have no known competing financial interests or personal relationships that could have appeared to influence the work reported in this paper.

Appendix A

$$P = IV_{ocv} - I^2R$$

$$P = \left[\frac{-1}{R}\left(\frac{W}{Q} - V_{ocv}\right)\right]V_{ocv} - \left[\frac{-1}{R}\left(\frac{W}{Q} - V_{ocv}\right)\right]^2 R$$

$$P = -\frac{W\,V_{ocv}}{RQ} + \frac{V_{ocv}^2}{R} - \left(-\frac{W}{RQ} + \frac{V_{ocv}}{R}\right)^2 R$$

$$P = -\frac{W\,V_{ocv}}{RQ} + \frac{V_{ocv}^2}{R} - \left(\frac{W^2}{R^2Q^2} + \frac{V_{ocv}^2}{R^2} - 2\cdot\frac{W\,V_{ocv}}{R^2\,Q}\right)R$$

$$P = -\frac{W\,V_{ocv}}{RQ} + \frac{V_{ocv}^2}{R} - \frac{W^2}{RQ^2} - \frac{V_{ocv}^2}{R} + 2\cdot\frac{W\,V_{ocv}}{RQ}$$

$$P = -\frac{W\,V_{ocv}}{RQ} - \frac{W^2}{RQ^2} + 2\cdot\frac{W\,V_{ocv}}{RQ}$$

$$P = \frac{V_{ocv}}{RQ}\cdot W - \frac{1}{RQ^2}\cdot W^2$$

Appendix B

In this section, the statistical distributions of the nominal voltage, capacity and resistance of the cells under study are shown. In particular, Fig. 17 shows the statistical distribution, in terms of probability density function (pdf), of the nominal cell voltage for the three LIBs at the tested reference

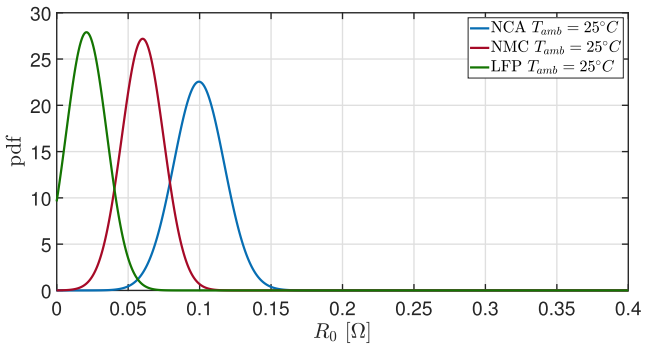

Fig. 19. Internal resistance distributions for the three LIBs at 25°. The internal resistance R_0 is identified over the pulse-train test.

temperatures.

Fig. 18 shows the pdf of the cell capacity for the three batteries at the tested reference temperatures, whereas Fig. 19 displays the bell-shaped distribution of the internal resistance at 25 °C (obtained from the pulse-train test).

Galavanostatic test data used in this paper are found in [46].

References

[1] Vetter M, Lux S. Rechargeable batteries with special reference to lithium-ion batteries. In: Letcher TM, editor. Storing Energy. Oxford: Elsevier; 2016. p. 205–25. https://doi.org/10.1016/B978-0-12-803440-8.00011-7 [chapter 11].

[2] Goldie-Scot L. A Behind the Scenes Take on Lithium-ion Battery Prices. BloombergNEF 2019. https://about.bnef.com/blog/behind-scenes-take-lithium-ion-battery-prices/.

[3] Bini M, Capsoni D, Ferrari S, Quartarone E, Mustarelli P. Rechargeable lithium batteries, vol. 4. Elsevier Ltd.; 2015. doi:10.1016/B978-1-78242-090-3.00001-8.

[4] Todeschini F, Onori S, Rizzoni G. An experimentally validated capacity degradation model for li-ion batteries in phevs applications. In: 8th IFAC Symposium on Fault Detection, Supervision and Safety of Technical Processes 2012; 2012.

[5] Le Fèvre P. The silent power of supercapacitors. Power Systems Design 2018. https://www.powersystemsdesign.com/articles/the-silent-power-of-supercapacitors/135/13510.

[6] Carter R, Cruden A, Hall P. Optimizing for efficiency or battery life in a battery/supercapacitor electric vehicle 2012;61:1526–33. https://doi.org/10.1109/TVT.2012.2188551.

[7] Mamun A, Liu Z, Rizzo D, Onori S. An Integrated Design and Control Optimization Framework for Hybrid Military Vehicle Using Lithium-Ion Battery and Supercapacitor as Energy Storage Devices. In: IEEE Transactions on Transportation Electrification, vol. 5. IEEE; 2019. p. 239–51. doi: 10.1109/TTE.2018.2869038.

[8] Khalil G. Challenges of hybrid electric vehicles for military applications. IEEE 2009:1–3. https://doi.org/10.1109/VPPC.2009.5289878.

[9] Moy K, Lee SB, Onori S. Characterization of duty cycles for the peak shaving electric grid energy storage application. In: Proceedings of the ASME 2020 Dynamic Systems and Control Conference; 2020.

[10] Irobot 510 packbot multi-mission robot. https://www.army-technology.com/projects/irobot-510-packbot-multi-mission-robot/.

[11] Gladiator tactical unmanned ground vehicle. Military Wiki; 2020. https://military.wikia.org/wiki/Gladiator_Tactical_Unmanned_Ground_Vehicle.

[12] Grabianowski E. How military robots work; 2005. https://science.howstuffworks.com/military-robot6.htm.

[13] Filipi Z, Fathy H, Hagena J, Knafl A, Ahlawat R, Liu J, et al. Engine-in-the-Loop Testing for Evaluating Hybrid Propulsion Concepts and Transient Emissions - HMMWV Case Study 2012. https://doi.org/10.4271/2006-01-0443.

[14] M-atv, American Special Ops; 2020. https://www.americanspecialops.com/vehicles/m-atv/.

[15] Oshkosh family of medium tactical vehicles (fmtv), Army Technology; 2010. https://www.army-technology.com/projects/oshkosh-family-of-medium-tactical-vehicles-fmtv/.

[16] Oshkosh hemtt heavy expanded mobility tactical truck, Army Technology. https://www.army-technology.com/projects/oshkosh-hemtt/.

[17] Line haul tractor, U.S. Army Acquisition Support Center; 2020. https://asc.army.mil/web/portfolio-item/cs-css-line-haul-tractor/.

[18] Ragone D. Review of Battery Systems for Electrically Powered Vehicles 1968;1:1–8. https://doi.org/10.4271/680453.

[19] Zschornak M, Meutzner F, Lück J, Latz A, Leisegang T, Hanzig J, Nentwich M, et al. Fundamental principles of battery design. In: Physical Sciences reviews, vol. 3; 2018. doi:10.1515/psr-2017-0111.

[20] S.T.R. Chemical energy storage. In: Bindra H, Revankar S, editors. Storage and Hybridization of Nuclear Energy. Academic Press; 2019. p. 177–227 [chapter 6]. http://www.sciencedirect.com/science/article/pii/B9780128139752000065. doi: https://doi.org/10.1016/B978-0-12-813975-2.00006-5.

[21] Murray D, Hayes J. Cycle testing of supercapacitors for long-life robust applications, vol. 30. IEEE; 2015. p. 2505–16. doi: 10.1109/TPEL.2014.2373368.

[22] Buchmann I. How does a supercapacitor work? Cadex Electronics 2019. https://batteryuniversity.com/learn/article/whats_the_role_of_the_supercapacitor.

[23] Nagasubramanian G, Jungst R. Energy and power characteristics of lithium-ion cells. J Power Sources 1998;72(2):189–93. https://doi.org/10.1016/S0378-7753(97)02712-2.

[24] Ci Y, Briat O, Boulon L, Deletage J-Y, Martin C, Coccetti F, et al. Non-isothermal Ragone plots of Li-ion cells from datasheet and galvanostatic discharge tests. Appl Energy 2019;247:703–15. https://doi.org/10.1016/j.apenergy.2019.04.027.

[25] Krishna K, Abduh A, Sabih O, Yazami R. Temperature effect on ragone plots of lithium-ion batteries 2018;165:A674–9. https://doi.org/10.1149/2.0591803jes].

[26] Ji Y, Zhang Y, Wang C. Li-ion cell operation at low temperatures 2013;160:636–49. https://doi.org/10.1149/2.047304jes.

[27] Schupbach R, Balda J, Zolot M, Kramer B. Design methodology of a combined battery-ultracapacitor energy storage unit for vehicle power management 2003:88–93. https://doi.org/10.1109/pesc.2003.1218278.

[28] Lopes J, Pomilio J, Ferreira P. Optimal sizing of batteries and ultracapacitors for fuel cell electric vehicles. In: IECON Proceedings (Industrial Electronics Conference), no. 1. IEEE; 2011. p. 4603–8. doi:10.1109/IECON.2011.6120068.

[29] Zhang Y, Tang X, Qi Z, Liu Z. The Ragone plots guided sizing of hybrid storage system for taming the wind power. In: International Journal of Electrical Power and Energy Systems, vol. 65. Elsevier Ltd; 2015. p. 246–53. doi:10.1016/j.ijepes.2014.10.006.

[30] Pell W, Conway B. Quantitative modeling of factors determining Ragone plots for batteries and electrochemical capacitors. In: Journal of Power Sources, vol. 63; 1996. p. 255–66. doi:10.1016/S0378-7753(96)02525-6.

[31] Christen T, Carlen M. Theory of Ragone plots. Journal of Power Sources 2000;91:210–6. https://doi.org/10.1016/S0378-7753(00)00474-2.

[32] Fuller M. A battery model for constant-power discharge including rate effects. In: Energy Conversion and Management, vol. 88; 2014. p. 199–205. doi: 10.1016/j.enconman.2014.08.015.

[33] Verbrugge M, Ying R. Energy vs power relationship for lithium ion cells over a broad range of temperatures and power densities. In: Journal of The Electrochemical Society, vol. 154; 2007. p. 949–56. doi:10.1149/1.2767410.

[34] Datasheet - ncr-18650b, Panasonic. https://www.imrbatteries.com/content/panasonic_ncr18650b-2.pdf.

[35] Product specification rechargeable lithium ion battery model inr21700 m50 18.20wh, LG Chem, https://dnkpower.com/wp-content/uploads/2019/02/LG-INR21700-M50-Datasheet.pdf.

[36] Nanophosphate high power lithium ion cell anr26650m1-b, A123 Systems; 2012. https://www.batteryspace.com/prod-specs/6610.pdf.

[37] Allam A, Onori S. Characterization of aging propagation in lithium-ion cells based on an electrochemical model. In: 2016 American Control Conference (ACC); 2016. p. 3113–8. https://doi.org/10.1109/ACC.2016.7525396.

[38] Onori S, Manenti A, Guezennec Y. New pba battery modeling structure and validation capturing the peukert effect. In: 8th International Conference on Lead-Acid Batteries LABAT; 2011.

[39] Datasheet - BC Series Ultracapacitors, Maxwell Technologies. p. 1–5. https://www.maxwell.com/images/documents/bcseries_ds_1017105.pdf.

[40] Rizoug N, Feld G, Barbedette B. Hybrid supply using supercapacitors for start & stop vehicles. In: 2010 Emobility - Electrical Power Train, EEPT 2010. IEEE; 2010. p. 1–6. doi: 10.1109/EMOBILITY.2010.5668058.

[41] Vehicle and Fuel Emissions Testing - Dynamometer Drive Schedules, United States Environmental Protection Agency. https://www.epa.gov/vehicle-and-fuel-emissions-testing/dynamometer-drive-schedules.

[42] Sherman D. Drag Queens: Aerodynamics Compared. Five slippery cars enter a wind tunnel; one slinks out a winner. Car and Driver 2014. https://www.caranddriver.com/features/a15108689/drag-queens-aerodynamics-compared-comparison-test/.

[43] Meyer D. Tires and Passenger Vehicle Fuel Economy. Washington, DC: The National Academies Press; 2006. doi: 10.17226/11620.

[44] Hayes J, Goodarzi G. Electric Powertrain: Energy Systems, Power Electronics and Drives for Hybrid, Electric and Fuel Cell Vehicles. Wiley; 2018. https://books.google.com/books?id=tshQDwAAQBAJ.

[45] Onori S, Serrao L, Rizzoni G. Hybrid electric vehicles: Energy management strategies. Springer; 2016. doi: https://doi.org/10.1007/978-1-4471-6781-5.

[46] Catenaro E, Onori S. Experimental data of lithium-ion batteries under galvanostatic discharge tests at different rates and temperatures of operation. In: Data in Brief; 2021.